

Beam Prediction Based on Multimodal Large Language Models

Tianhao Mao, *Student Member, IEEE*, Le Liang, *Member, IEEE*, Jie Yang, *Member, IEEE*,
Xiao Li, *Member, IEEE*, and Shi Jin, *Fellow, IEEE*

Abstract—Accurate beam prediction is a key enabler for next-generation wireless communication systems. In this paper, we propose a multimodal large language model (LLM)-based beam prediction framework that effectively utilizes contextual information, provided by sensory data including RGB camera images and LiDAR point clouds. To effectively fuse heterogeneous modalities, we design specialized modality encoders together with a beam-guided attention masking mechanism and a high-frequency temporal alignment strategy, enabling robust cross-modal feature integration under dynamic environments. Furthermore, we construct a large-scale multimodal dataset for communication, named Multimodal-Wireless, which covers diverse weather and traffic conditions with high-fidelity ray-tracing labels. Extensive simulation results demonstrate that the proposed approach significantly reduces the reliance on oracle angle-of-departure knowledge and consistently outperforms state-of-the-art multimodal LLM-based beam prediction methods in terms of beam accuracy and communication performance, improving the average Top-1 accuracy to 80.8% and the average normalized gain to 89.1%.

Index Terms—Beam prediction, context-aware communication, multimodal dataset, multimodal large language model.

I. INTRODUCTION

THE performance of future communication systems, particularly those employing massive multiple-input multiple-output (MIMO) at high frequencies, hinges on precise beam alignment. However, maintaining this alignment under user mobility presents a fundamental dilemma. Conventional methods typically rely on exhaustive beam sweeping or reactive recovery protocols, which incur prohibitive latency and consume substantial signaling overhead. Such heavy training burdens severely degrade spectral efficiency and often lead to service interruptions when the channel changes faster than the feedback loop. To break these bottlenecks, a paradigm shift from reactive to proactive management is essential, necessitating a dynamic understanding of the operational context derived from environmental sensing [2]. By leveraging such context to anticipate optimal beams before link degradation occurs, proactive beam prediction becomes a key enabler for

reducing training overhead and ensuring seamless connectivity in next-generation networks.

To achieve such proactivity, context-aware communication strategies have been proposed to mitigate the overhead inherent to millimeter-wave (mmWave) systems [3]–[5]. While some strategies rely on user feedback or assume perfect knowledge of historical angle of departure (AoD) [5], such information is often unavailable or delayed at the base station (BS). In contrast, local sensory data derived from on-site RGB cameras and light detection and ranging (LiDAR) is readily accessible and provides rich geometric and visual cues about the propagation environment. Hence, we focus on leveraging exclusively BS-side sensing data as a practical and deployable solution for robust context-aware prediction.

Leveraging such multimodal data, several studies have emerged on deep learning-based physical layer techniques [6]–[11]. Pioneering works have demonstrated the feasibility of using visual, positional, and LiDAR data to accelerate beam selection or predict optimal beams [6], [8]. Some approaches have further introduced attention mechanisms to fuse these heterogeneous features [9]. However, due to their limited parameter scale and architectural constraints, these traditional learning-based models, like long short-term memory (LSTM), often struggle to capture complex spatial-temporal dependencies. Consequently, existing small-scale learning-based predictors often fail to generalize effectively under dynamic environmental shifts and unseen scenarios [12].

To address generalization issues, recent work [5] has adopted large language models (LLMs) for beam prediction, demonstrating significantly improved robustness compared to conventional methods. However, this approach relies on historical channel angles rather than raw sensory data. Furthermore, simply applying existing multimodal LLMs—from foundational encoders like CLIP [13] and Imagebind [14] to systems like BLIP-2 [15] and Imagebind-LLM [16]—is insufficient. Current multimodal paradigms are designed to align semantically similar cross-modal data, whereas wireless applications require exploiting the heterogeneity where LiDAR, cameras, and channels carry distinct, complementary information. Therefore, we need a specialized multimodal LLM framework that performs complementary fusion, which inherently necessitates matched high-frequency, weather-diverse, and BS-side aligned training data.

Meanwhile, the development of such data-driven models depends heavily on specialized datasets. While sensing-centric datasets like OPV2V [17] and DAIR-V2X [18] and communication-focused ones like DeepMIMO [19] exist,

T. Mao, L. Liang, X. Li, and S. Jin are with the School of Information Science and Engineering, Southeast University, Nanjing 210096, China (e-mail: tianhao@seu.edu.cn; lliang@seu.edu.cn; li_xiao@seu.edu.cn; jinshi@seu.edu.cn). L. Liang is also with the Purple Mountain Laboratories, Nanjing 211111, China.

J. Yang is with the Key Laboratory of Measurement and Control of Complex Systems of Engineering, Ministry of Education, Southeast University, Nanjing 210096, China (e-mail: yangjie@seu.edu.cn).

This paper was accepted in part by the 2026 IEEE International Conference on Communications [1].

bridging the divide remains difficult. Efforts such as e-Flash [20], ViWi [21] and DeepSense 6G [22] have begun to integrate these domains, yet persistent limitations remain, including the omission of adverse weather conditions, a reliance on low-frequency received power, or a lack of precise ray-tracing alignment. These gaps hinder the training of models that can withstand realistic environmental impairments like rain or fog.

In this paper, we address these key challenges by proposing a novel multimodal LLM framework that operates exclusively on readily available, BS-side sensing data. Our architecture utilizes modality-specific encoders and a unique fusion interface that preserves high-frequency channel information by upsampling sensory features. Trained and tested on the uniquely developed Multimodal-Wireless dataset, our model significantly outperforms the state-of-the-art approach. Our main contributions are presented in detail as follows:

- We propose a multimodal LLM-based framework for robust beam prediction, featuring a beam-guided attention mechanism (BGAM) and high-frequency temporal alignment. Our architecture utilizes modality-specific encoders, integrating PointPillars for LiDAR and a cross-attention-based RGB encoder. To resolve spatial ambiguity in multi-vehicle scenarios, BGAM leverages historical beam indices to dynamically guide the LiDAR encoder's attention. This allows the model to selectively extract target-specific geometric features. Also, instead of down-sampling, we adopt a temporal alignment strategy that upsamples sensory features to match the high-frequency (100 Hz) channel information, thereby preserving critical temporal resolution.
- We introduce Multimodal-Wireless, a large-scale, open-source multimodal dataset for joint sensing and communication research. The dataset provides channel state information sampled at 100 Hz, alongside five other sensor modalities: LiDAR, RGB and depth cameras, inertial measurement unit (IMU), and radar. To facilitate practical implementation and temporal alignment, these modalities can be flexibly downsampled. Crucially, Multimodal-Wireless encompasses diverse weather conditions, including sunny, rainy, and foggy scenarios, enabling robust evaluation of weather-induced impairments. The dataset is also extensible, allowing researchers to easily generate and contribute their own data.
- We validate our multimodal LLM-based model on the Multimodal-Wireless dataset, demonstrating that the integration of multimodal sensor data—particularly LiDAR—with beam indices significantly enhances long-term beam prediction accuracy. Notably, our proposed framework achieves a higher normalized gain than a state-of-the-art LLM-based algorithm that presumes perfect knowledge of historical AoD and beam indices. By eliminating the need for AoD information, our approach overcomes a critical practical limitation and offers a viable and robust solution for real-world deployment.

The rest of the paper is organized as follows. In Section II, we first formulate the long-term beam prediction problem. We



Fig. 1. Illustration of beam prediction in MIMO communications with multimodal data.

then clarify the network structure in Section III, including the modality encoder, modality interface, and output projection. The Multimodal-Wireless dataset used for training and testing the model is introduced in Section IV. In Section V, we present comprehensive simulation results related to multi-modality, weather conditions, and robustness. Finally, we conclude the paper in Section VI.

The notations used are defined as follows. \mathbf{a} and \mathbf{A} denote a column vector and a matrix, respectively, and $\mathbf{A}[i, j]$ refers to the entry at the i -th row and j -th column of \mathbf{A} . The transpose and conjugate transpose of \mathbf{A} is denoted by \mathbf{A}^T and \mathbf{A}^H , respectively. The floor of a real number x , denoted by $\lfloor x \rfloor$, is the greatest integer smaller than or equal to x . $|y|$ represents the absolute value of a complex number y .

II. PROBLEM FORMULATION

We consider a dynamic downlink system where a roadside unit (RSU) acts as the BS transmitter, and a vehicle is the user receiver, as illustrated in Fig. 1. The RSU is equipped with an N_t -antenna uniform linear array (ULA), and the vehicle with an N_r -antenna ULA. The inter-element spacing d for both arrays is set as $\lambda/2$, where λ is the carrier wavelength. In addition, the RSU collects local sensory data, among which it utilizes LiDAR and RGB camera data for physical layer design. The communication setup yields a geometric multipath channel whose frequency-domain representation for the k -th subcarrier at time step n is expressed as [23]:

$$\mathbf{H}_{n,k} = \sqrt{\frac{N_t N_r}{L_n}} \sum_{l=1}^{L_n} \alpha_{n,l} \mathbf{a}_r(\theta_{n,l}) \mathbf{a}_t^H(\phi_{n,l}) e^{-j2\pi f_k \tau_{n,l}}. \quad (1)$$

Here, L_n represents the number of multi-paths at time step n . Each path is characterized by a complex gain $\alpha_{n,l}$, delay $\tau_{n,l}$, angles of arrival (AoA) $\theta_{n,l}$, and AoD $\phi_{n,l}$. For an orthogonal frequency division multiplexing (OFDM) system with K subcarriers and Δf subcarrier spacing, f_k is the baseband frequency of the k -th subcarrier and satisfies $f_k = (k - \frac{K+1}{2})\Delta f$. The steering vectors are defined as:

$$\begin{aligned} \mathbf{a}_t(\theta) &= \left[1, e^{j2\pi d \sin \theta / \lambda}, \dots, e^{j2\pi (N_t - 1) d \sin \theta / \lambda} \right]^T, \\ \mathbf{a}_r(\phi) &= \left[1, e^{j2\pi d \sin \phi / \lambda}, \dots, e^{j2\pi (N_r - 1) d \sin \phi / \lambda} \right]^T. \end{aligned} \quad (2)$$

The system sends a single data stream with a precoder $\mathbf{f} \in \mathbb{C}^{N_t \times 1}$ at the RSU and a combiner $\mathbf{w} \in \mathbb{C}^{N_r \times 1}$ at the vehicle. Thus, the received signal can be written as

$$y_{n,k} = \mathbf{w}^H \mathbf{H}_{n,k} \mathbf{f} x_{n,k} + s_{n,k}, \quad (3)$$

where $x_{n,k}$ and $y_{n,k}$ are the signal transmitted and received at the n -th time step and the k -th subcarrier, and $s_{n,k}$ is the communication noise, an independent and identically distributed (i.i.d.) circularly symmetric complex Gaussian random variable with zero mean and a variance of σ^2 .

We consider an analog beamforming architecture with a single radio frequency chain, with both \mathbf{f} and \mathbf{w} selected from a predefined discrete fourier transform (DFT) codebook. For a codebook of size Q , the q -th candidate beamformer is expressed as

$$\mathbf{f}(q) = \frac{1}{\sqrt{N_t}} [1, e^{j2\pi q/Q}, \dots, e^{j2\pi(N_t-1)q/Q}]^T. \quad (4)$$

The primary task addressed in this work is to predict the optimal transmit beam indices for the next W time steps, $\{\hat{q}_m\}_{m=1}^W$, based on historical information from the past P time steps, including optimal transmit beam indices, LiDAR point clouds, and camera images. Mathematically, we aim to find the series of beam indices $\{\hat{q}_1, \dots, \hat{q}_m, \dots\}$ that achieve the maximum sum of normalized beamforming gain for future W time steps, which is expressed by

$$\max_{\{\hat{q}_m\}_{m=1}^W} \frac{1}{W} \sum_{m=1}^W G(\hat{q}_m), \quad (5)$$

where $G(\hat{q}_m)$ is the normalized gain of the future time step m , defined by

$$G(\hat{q}_m) = \frac{|\mathbf{w}(p_m^*)^H \mathbf{H}_m \mathbf{f}(\hat{q}_m)|^2}{|\mathbf{w}(p_m^*)^H \mathbf{H}_m \mathbf{f}(q_m^*)|^2}, \quad (6)$$

with $\mathbf{H}_m = \frac{1}{K} \sum_{k=1}^K \mathbf{H}_{m,k}$ representing the channel matrix averaged over all K subcarriers. p_m^* and q_m^* denote the optimal precoder and combiner beam indices at future time step m , respectively, determined via an exhaustive search over the codebook to maximize the received signal power:

$$(p_m^*, q_m^*) = \arg \max_{p_m, q_m \in \{0, \dots, Q-1\}} |\mathbf{w}(p_m)^H \mathbf{H}_m \mathbf{f}(q_m)|^2. \quad (7)$$

III. MULTIMODAL LLM-BASED BEAM PREDICTION

In this section, we detail our multimodal LLM-based method, comprising two key components: a modality encoder for feature extraction of each data type, and a modality interface for temporal alignment and subsequent fusion of these multimodal features. We note that by reprogramming an embedding-visible LLM, the optimal transmit beam prediction can be performed without fine-tuning the backbone model [5]. The structure of our method is presented in Fig. 2.

A. Modality Encoder

Unlike traditional encoders that align the semantic space of different modalities [13], our approach preserves the intrinsic heterogeneity of each modality. This is designed to exploit complementary information, allowing the strengths of one modality to compensate for the weaknesses of another. To achieve this, we design modality-specific encoders for heterogeneous modality data to extract the diverse features for the beam prediction task, ensuring tailored processing for each modality before its features are interpreted by the LLM.

1) *Beam Index*: We use past optimal beam indices $\mathbf{q}_P^* \in \mathbb{R}^{P \times 1}$ from the BS side as historical observations. Given that different codebook sizes lead to distinct ranges of beam indices, we adopt a pre-processor [5] to normalize the past optimal beam index sequence \mathbf{q}_P^* by

$$\mathbf{q}^* = \frac{\mathbf{q}_P^*}{Q}, \quad (8)$$

in order to enhance the generalization of our model.

Regarding feature embedding, we adopt an embedding layer to map $\mathbf{q}^* \in \mathbb{R}^{P \times 1}$ into $\mathbf{U}_B \in \mathbb{R}^{P \times d_m}$, where d_m is the unified dimension within the modality encoding stage, preparing the features for the subsequent modality interface, introduced in Section III-B. Specifically, the layer uses a one-dimensional convolution to project input features into a target embedding space, and processes the input sequence \mathbf{q}^* with d_m convolution kernels of size 3, which captures local contextual information from neighboring time steps when creating the embedding for each time step.

2) *LiDAR*: The raw LiDAR point cloud, comprising sparse and unordered points within the three-dimensional (3D) perception space, is processed by a Pointpillar network [24], a self-designed beam-guided attention masking (BGAM) and a cross-attention layer in sequence.

Pointpillar: The point cloud is first processed by a frozen pre-processor that adopts the first two stages of the PointPillars architecture, i.e., a feature encoder and a 2D convolutional backbone, transforming the point cloud into a sparse bird's eye view (BEV). The process is illustrated in Fig. 3. Specifically, the 3D perception space of LiDAR is first discretized into vertical pillars by gridding the $x-y$ plane. Points within each non-empty pillar are augmented into 9-dimensional features by incorporating offsets from the pillar's center and the points' centroid. To mitigate inherent data sparsity, sampling a bounded number of pillars and points yields a fixed-size dense tensor. PointNet [25] then extracts point-level features, which are subsequently aggregated into a unified pillar representation via point-wise max-pooling. By scattering these features back to their original 2D grid locations, a pseudo-image is constructed. Finally, a 2D convolutional neural network processes this pseudo-image, employing a top-down pathway to extract decreasing-resolution features and an upsampling module to concatenate them into a multi-scale representation.

We note here that the weights for these two stages are initialized from a public implementation [17] and remain frozen during training. The output of this pre-processing is the BEV feature map $\mathbf{X}_L \in \mathbb{R}^{C_L \times H_L \times W_L}$.

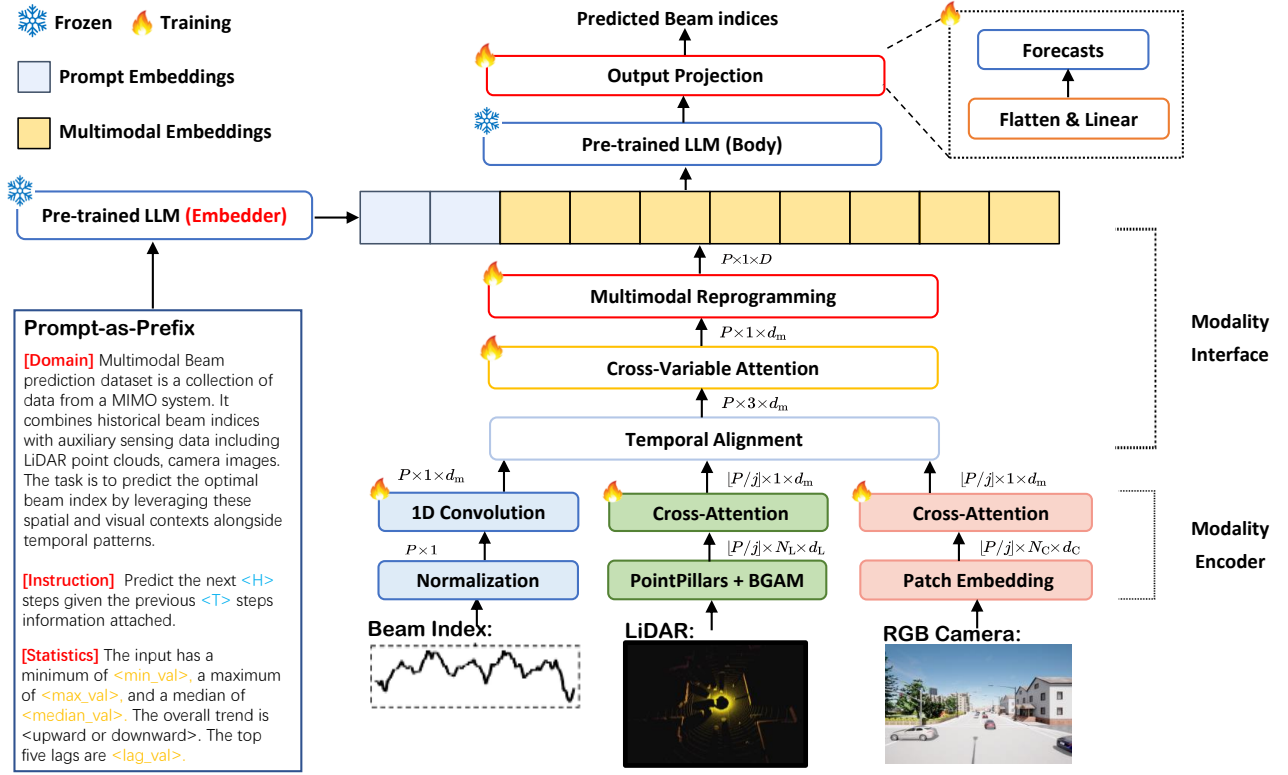


Fig. 2. The structure of the multimodal LLM-based beam prediction network.

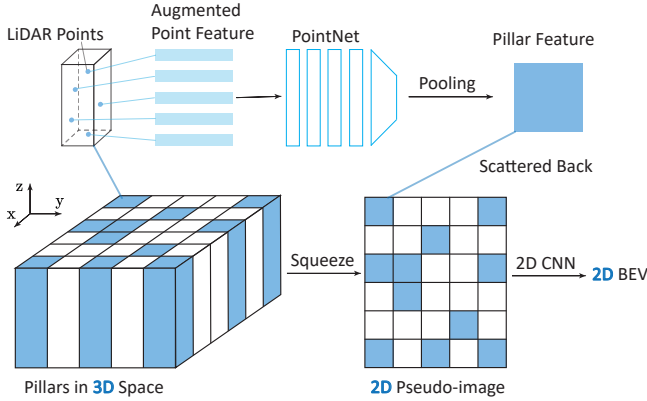


Fig. 3. The 3D to 2D BEV process of Pointpillar [24].

Beam-Guided Attention Masking: A key challenge in multimodal beam prediction is bridging the semantic gap between the abstract communication modality, i.e., discrete beam indices, and the rich spatial information from sensory data. To address this, we introduce a BGAM module that injects inductive bias by enforcing the physical constraints of the communication channel directly onto the BEV feature. This acts as a hard attention mechanism, guiding the model to focus solely on the spatial region relevant to a specific beam.

The BGAM process operates as follows. For each historical beam index $q \in \{0, \dots, Q-1\}$, we first map it to its corresponding continuous physical AoD, ϕ_q . This mapping is derived by aligning the phase progression of the n -th antenna element in the q -th DFT beamformer, as defined in (4), with

the phase of the physical steering vector for a ULA, as defined in (2). Assuming a standard inter-element spacing of half a wavelength, i.e., $d = \lambda/2$, this alignment yields a direct relationship between the beam index and its pointing angle. To ensure the generated beams cover the full angular spectrum from -90° to $+90^\circ$, the codebook is designed such that the sine of the angle is sampled uniformly in the range $[-1, 1]$. This results in the following mapping:

$$\sin(\phi_q) = \frac{2(q+0.5)}{Q} - 1. \quad (9)$$

From this, the center angle for each beam is given by

$$\phi_q = \arcsin\left(\frac{2(q+0.5)}{Q} - 1\right). \quad (10)$$

To generate the spatial mask, we define an angular range $[\phi_q - \delta_q, \phi_q + \delta_q]$, where δ_q is the corresponding adaptive angular half-width, which satisfies

$$\sin(\phi_q + \delta_q) - \sin(\phi_q - \delta_q) \propto \frac{2}{Q}. \quad (11)$$

Concurrently, we compute a static angle grid, $\Theta \in \mathbb{R}^{H_L \times W_L}$, where each element $\Theta[i, j]$ stores the pre-calculated angle of the center of the BEV grid cell (i, j) relative to the RSU. A binary spatial mask $\mathbf{M} \in \{0, 1\}^{H_L \times W_L}$ is then generated for the beam index q according to:

$$\mathbf{M}[i, j] = \begin{cases} 1, & \text{if } \Theta[i, j] \in [\phi_q - \delta_q, \phi_q + \delta_q], \\ 0, & \text{otherwise.} \end{cases} \quad (12)$$

This mask isolates the spatial region covered by the beam. The high-level BEV feature map \mathbf{X}_L can be viewed as a grid of

feature vectors, where $\mathbf{x}_{i,j} \in \mathbb{R}^{C_L}$ denotes the feature representation at the spatial location (i, j) . The masking operation is applied spatially as:

$$\hat{\mathbf{x}}_{i,j} = \mathbf{x}_{i,j} \cdot \mathbf{M}[i, j]. \quad (13)$$

Here, the scalar value $\mathbf{M}[i, j] \in \{0, 1\}$ acts as a gate, either preserving or suppressing the entire feature vector at each grid cell based on the beam’s coverage. Subsequently, by spatially stacking the masked feature vectors $\hat{\mathbf{x}}_{i,j}$ across all grid cells, we reconstruct the refined LiDAR BEV feature map $\tilde{\mathbf{X}} \in \mathbb{R}^{C_L \times H_L \times W_L}$, which serves as the beam-aware representation for downstream prediction. By zeroing out features outside the beam’s direct line-of-sight (LOS), this BGAM process significantly prunes the feature space, reducing noise and computational complexity for downstream components. More importantly, it forces an explicit alignment between the communication state and the environmental perception, improving the model’s interpretability.

Cross-Attention Layer: To transform the 2D spatial representation into a format compatible with the attention-based mechanism, the resulting tensor $\tilde{\mathbf{X}}$ is then flattened into $\tilde{\mathbf{X}}_L \in \mathbb{R}^{N_L \times C_L}$, with $N_L = H_L \times W_L$. We then employ a cross-attention mechanism to summarize these features using a learnable query vector $\mathbf{q}_L \in \mathbb{R}^{1 \times C_L}$. The operation is:

$$\mathbf{u}_L = \text{CrossAttention}(\mathbf{q}_L, \tilde{\mathbf{X}}_L, \tilde{\mathbf{X}}_L), \quad (14)$$

where $\mathbf{u}_L \in \mathbb{R}^{1 \times d_m}$ is the final embedded feature.

Our cross-attention is implemented with a standard multi-head mechanism with N_h heads. First, the query, key, and value are linearly projected using shared weight matrices $\mathbf{W}_q \in \mathbb{R}^{C_L \times d_m}$, $\mathbf{W}_k \in \mathbb{R}^{C_L \times d_m}$, and $\mathbf{W}_v \in \mathbb{R}^{C_L \times d_m}$ as

$$\begin{aligned} \mathbf{q}' &= \mathbf{q}_L \mathbf{W}_q, \\ \mathbf{K}' &= \tilde{\mathbf{X}}_L \mathbf{W}_k, \\ \mathbf{V}' &= \tilde{\mathbf{X}}_L \mathbf{W}_v. \end{aligned} \quad (15)$$

The resulting matrices $\mathbf{q}' \in \mathbb{R}^{1 \times d_m}$, $\mathbf{K}' \in \mathbb{R}^{N_L \times d_m}$, and $\mathbf{V}' \in \mathbb{R}^{N_L \times d_m}$ are then split into N_h heads. For each head $s \in \{1, \dots, N_h\}$, the inputs are $\mathbf{Q}_s \in \mathbb{R}^{1 \times d}$, $\mathbf{K}_s \in \mathbb{R}^{N_L \times d}$, and $\mathbf{V}_s \in \mathbb{R}^{N_L \times d}$, where $d = d_m/N_h$ is the dimension of each head. The attention output for head s can be written as

$$\mathbf{u}_s = \text{Softmax} \left(\frac{\mathbf{q}_s \mathbf{K}_s^T}{\sqrt{d}} \right) \mathbf{V}_s. \quad (16)$$

Finally, the outputs of all heads are concatenated to form

$$\mathbf{u}_L = \text{Concat}(\mathbf{u}_1, \dots, \mathbf{u}_{N_h}), \quad (17)$$

which is the feature embedding of a single LiDAR point cloud. To align with the dimensions of the beam index embedding \mathbf{U}_B , the encoded features of the undersampled LiDAR point clouds from the past P time steps are replicated and concatenated to construct the historical LiDAR feature embedding $\mathbf{U}_L \in \mathbb{R}^{P \times d_m}$. The detailed process is presented in Section III-B.

3) *RGB Camera:* The visual feature encoder is designed to extract high-dimensional semantic representations from raw camera observations. We employ a pre-trained vision transformer (ViT-B/16) [26] as the structural backbone.

To preserve the spatial integrity and aspect ratio of the input images, we implement a multi-stage preprocessing pipeline. Specifically, an input image is first isotropically resized such that its shorter dimension matches the model’s input requirement, i.e., 224 pixels. Subsequently, a center crop is applied to produce a fixed-size tensor $\mathbf{X}_C \in \mathbb{R}^{3 \times 224 \times 224}$. This strategy minimizes geometric distortion compared to naive resizing, thereby maintaining the semantic consistency of local features.

The preprocessed image is partitioned into $N_p = 224^2/Z^2$ non-overlapping patches with a patch size of Z . Each patch is flattened and projected into a $d_C = 768$ dimensional latent space. Let Ω_0 be the input sequence to the transformer encoder, defined by

$$\Omega_0 = [\mathbf{x}_{\text{cls}}; \mathbf{x}_1 \mathbf{E}_p; \mathbf{x}_2 \mathbf{E}_p; \dots; \mathbf{x}_{N_p} \mathbf{E}_p] + \mathbf{E}_{\text{pos}}, \quad (18)$$

where $\mathbf{x}_{\text{cls}} \in \mathbb{R}^{1 \times (3Z^2)}$ denotes the classification token, and $\mathbf{x}_i \in \mathbb{R}^{1 \times (3Z^2)}$ is the flattened patch. $\mathbf{E}_p \in \mathbb{R}^{(3Z^2) \times d_C}$ is the patch embedding projection and $\mathbf{E}_{\text{pos}} \in \mathbb{R}^{(N_p+1) \times d_C}$ denotes the learnable positional embeddings.

The sequence Ω_0 is then forwarded through the transformer encoder, which consists of 12 layers of multi-head self-attention and multi-layer perceptron blocks. Let $\Omega \in \mathbb{R}^{(N_p+1) \times d_C}$ denote the output hidden states from the final layer. Instead of utilizing the global class token $\Omega^{(0)}$ corresponding to \mathbf{x}_{cls} for image-level classification, we extract the sequence of transformed patch tokens to preserve spatial information. The resulting feature map, $\tilde{\mathbf{X}}_C \in \mathbb{R}^{N_p \times d_C}$, is obtained by slicing the output tensor:

$$\tilde{\mathbf{X}}_C = \Omega[2 : N_p + 1, :]. \quad (19)$$

This feature map $\tilde{\mathbf{X}}_C$ provides a dense, spatially-aware representation of the scene, where each token encapsulates local semantic information conditioned on the global context through the self-attention mechanism.

For feature embedding, we adopt the same cross-attention mechanism as the LiDAR feature embedding for RGB images, along with the subsequent replication and concatenation process to transform the feature embeddings of the undersampled RGB images into historical image feature embedding $\mathbf{U}_C \in \mathbb{R}^{P \times d_m}$, as detailed in the following subsection.

B. Modality Interface

Although tailored representations are extracted from heterogeneous modalities, the inherent sampling rate disparity between the sensors and the beam index causes LiDAR and camera features to remain asynchronous with the beam index features. Furthermore, such non-textual representations cannot be directly ingested by a natural language-pretrained LLM. To bridge this gap, the modality interface is designed to synchronize, fuse, and translate these disparate data streams. First, it addresses the challenge of different sensor sampling rates by temporally aligning the lower-frequency perceptual data to the high-frequency timeline of the communication

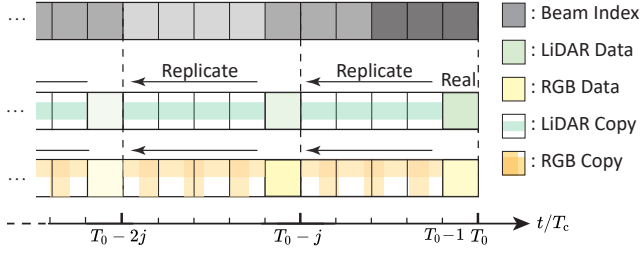


Fig. 4. Temporal alignment strategy for the modality interface.

channel. Subsequently, a cross-modality attention layer is employed to aggregate the complementary spatial and temporal messages from all aligned modalities. Finally, a modality reprogramming module translates the fused multimodal tensor into language-aligned embeddings. This vital transformation effectively projects the physical sensory data into a unified vocabulary space, enabling the pre-trained LLM to reason comprehensively about the multimodal environment.

1) *Temporal Alignment*: A critical challenge in multimodal fusion is handling the disparate sampling rates of different sensors. Departing from conventional approaches that often downsample to the lowest common frequency—sacrificing temporal resolution—or simply ignore these asynchronies [8], [9], we introduce a strategy that preserves high-frequency information while respecting real-world data availability.

Our alignment methodology is anchored to the high-frequency timeline of the communication channel with a sampling period T_c . Lower-frequency data from perceptual sensors, such as LiDAR and cameras with a period T_{pc} , are up-sampled to match this reference timeline. Each sensor measurement corresponds to a window of $j = T_{pc}/T_c$ channel steps. Since a typical LiDAR sampling period of 100 ms or 50 ms is an integer multiple of the standard 10 ms 5G NR frame duration, this ratio naturally results in an integer value of $j = 10$ or $j = 5$, respectively. The cornerstone of our approach is the enforcement of causality: each sensor measurement is aligned to the end of its acquisition window, faithfully modeling real-world conditions and ensuring data is used after it becomes available.

This principle directly governs the construction of our multimodal input tensors. As illustrated in Fig. 4, for a history of P time steps, the $\lfloor P/j \rfloor$ sparse encoded features for LiDAR and camera are temporally aligned with the high-frequency beam index sequence via backward replication. Specifically, each “real” feature available at every j -th time step is retrospectively copied to fill the $j - 1$ preceding time steps within the same sampling interval. This process ensures that the resulting LiDAR sequence $\mathbf{U}_L \in \mathbb{R}^{P \times d_m}$ and camera sequence $\mathbf{U}_C \in \mathbb{R}^{P \times d_m}$ are temporally dense and synchronized with the beam index sequence $\mathbf{U}_B \in \mathbb{R}^{P \times d_m}$ of length P . By expanding these feature embeddings along a newly introduced modality dimension, we obtain $\mathbf{U}'_B, \mathbf{U}'_L,$ and $\mathbf{U}'_C \in \mathbb{R}^{P \times 1 \times d_m}$. Subsequently, concatenating these tensors along the modality dimension yields

$$\mathbf{U} = \text{Concat}(\mathbf{U}'_B, \mathbf{U}'_L, \mathbf{U}'_C). \quad (20)$$

The obtained tensor, $\mathbf{U} \in \mathbb{R}^{P \times 3 \times d_m}$, represents a temporally coherent and causally-sound fusion of all modalities, ready for processing by the subsequent cross-modality attention layers.

2) *Cross-Modality Attention*: To analyze the features in \mathbf{U} and aggregate messages from all modalities, we then employ a cross-modality attention layer. It utilizes a learnable query tensor $\mathbf{R} \in \mathbb{R}^{P \times 1 \times d_m}$ to aggregate information, with \mathbf{U} serving as both key and value:

$$\mathbf{B} = \text{CrossAttention}(\mathbf{R}, \mathbf{U}, \mathbf{U}). \quad (21)$$

The resulting tensor $\mathbf{B} \in \mathbb{R}^{P \times 1 \times d_m}$ is a fused representation that is then passed to the next module. The layer itself is built upon a standard multi-head attention architecture, as discussed in Section III-A.

3) *Modality Reprogramming*: The fused feature tensor \mathbf{B} is a powerful representation, which, however, cannot be directly processed by an LLM pre-trained on natural language. To bridge this gap, we introduce a modality reprogramming module that translates \mathbf{B} into language-aligned embeddings, enabling the LLM to reason about the fused multimodal data.

This reprogramming is achieved by projecting \mathbf{B} into a compact, continuous semantic subspace derived from the LLM’s vocabulary. For computational efficiency, we avoid computing cross-attention over the entire vocabulary embedding matrix $\mathbf{E} \in \mathbb{R}^{V \times D}$, where V and D represents the vocabulary size and the hidden dimension of the LLM, respectively. Instead, we apply a learnable linear projection to \mathbf{E} to construct a condensed set of latent text prototypes, $\mathbf{E}' \in \mathbb{R}^{V' \times D}$ (where $V' \ll V$). Unlike manually curated, discrete text prompts (e.g., “strong signal”), these data-driven virtual tokens act as learnable semantic anchors. This allows the model to automatically map complex, high-dimensional multimodal inputs to the most optimal language-aligned concepts during the end-to-end optimization process. Specifically, the translation of \mathbf{B} is implemented with a multi-head cross-attention layer, where the text prototypes \mathbf{E}' act as both key and value, and $\mathbf{B}' \in \mathbb{R}^{P \times d_m}$ serves as the query, generated by squeezing the redundant modality dimension in \mathbf{B} . The operation is defined as

$$\mathbf{Z} = \text{CrossAttention}(\mathbf{B}', \mathbf{E}', \mathbf{E}'), \quad (22)$$

where the output $\mathbf{Z} \in \mathbb{R}^{P \times D}$ is the reprogrammed feature sequence. These vectors now reside in the same embedding space as the LLM’s vocabulary, making them a suitable input for the LLM backbone.

4) *Prompt-as-Prefix*: To guide the LLM’s reasoning process and anchor its general capabilities to the specifics of the beam prediction task, we construct a structured natural language prompt for each input sample according to [5]. This prompt is prepended as a prefix to the reprogrammed feature sequence, a technique we term prompt-as-prefix. The combined sequence is then fed into the LLM backbone.

Each prompt is a structured string that concatenates several key pieces of information, designed to provide a comprehensive context for the model:

- **Dataset Description**: A static text describing the overall dataset, designed to be: “Beam prediction dataset is a collection of millisecond data from a multiple-input

single-output system, describing the movement of beam direction over time, which typically remains constant within several time steps.”

- **Task Description:** An explicit instruction defining the forecasting goal, such as “forecast the next W steps given the previous P steps information,” where P is the look-back window and W is the prediction horizon.
- **Instance-Specific Statistics:** A dynamic summary of the current input sequence’s statistical properties, including: basic statistics like the minimum, maximum, and median values of the beam indices; a textual description of the overall beam index trend (either “upward” or “downward”), determined by the sign of a trend metric; the top five most significant time intervals where the data shows the strongest repeating patterns, discovered by calculating how the time series correlates with its own past via Fast Fourier Transform.

This structured text is then passed through the pre-trained LLM’s tokenizer and embedding layer to generate a sequence of prompt embeddings, $\mathbf{P}_{\text{prom}} \in \mathbb{R}^{L_{\text{prom}} \times D}$, where L_{prom} denotes the token length of the prompt. This ensures that the prompt resides in the same semantic space as the LLM’s internal representations. Finally, the prompt embeddings are concatenated with the reprogrammed feature sequence \mathbf{Z} to form the unified input $\tilde{\mathbf{Z}} \in \mathbb{R}^{(L_{\text{prom}}+P) \times D}$:

$$\tilde{\mathbf{Z}} = \text{Concat}(\mathbf{P}_{\text{prom}}, \mathbf{Z}), \quad (23)$$

which is further processed by the LLM backbone.

C. Output Projection

The output of the LLM backbone, denoted as $\tilde{\mathbf{O}}_{\text{LLM}} \in \mathbb{R}^{P' \times D}$, is a sequence of high-dimensional hidden states, where P' is the length of the concatenated prompt and reprogrammed features. To transform these abstract representations into a concrete forecast, we design a dedicated prediction head.

First, we extract the feature vectors corresponding only to our original input sequence, discarding the outputs associated with the prompt prefix. This yields a matrix $\mathbf{O}_{\text{LLM}} \in \mathbb{R}^{P \times D}$. We then reduce the feature dimension from D to a smaller, intermediate dimension D_{ff} by selecting the initial components of each vector, which produces $\mathbf{O}'_{\text{LLM}} \in \mathbb{R}^{P \times D_{\text{ff}}}$.

The core of the prediction head is a linear projection layer that directly maps the flattened sequence of features to the desired prediction horizon. Specifically, \mathbf{O}'_{LLM} is flattened into a single long vector and then linearly projected to a vector of length W . This can be formulated as

$$\hat{\mathbf{y}}_W = \text{Flatten}(\mathbf{O}'_{\text{LLM}}) \cdot \mathbf{W}_{\text{out}} + \mathbf{b}_{\text{out}}, \quad (24)$$

where $\mathbf{W}_{\text{out}} \in \mathbb{R}^{(P \cdot D_{\text{ff}}) \times W}$ and $\mathbf{b}_{\text{out}} \in \mathbb{R}^W$ are the learnable weights and bias of the final linear layer.

Finally, the output $\hat{\mathbf{y}}_W$ is passed through a denormalization layer to revert the prediction to the original data scale, producing the final forecast $\hat{\mathbf{q}}_W$. The loss function is designed to minimize the mean-squared error between the predicted $\hat{\mathbf{q}}_W$ and the ground truth \mathbf{q}_W^* , which can be expressed as

$$\text{Loss} = \frac{1}{W} \sum_{m=1}^W (\hat{q}_m - q_m^*)^2. \quad (25)$$

IV. MULTIMODAL-WIRELESS DATASET

In this section, we briefly introduce Multimodal-Wireless, a large-scale open-source dataset for multimodal sensing and communication research. The dataset is collected in a dynamic vehicular environment, where vehicles and RSUs gather multimodal data for collaborative perception. Alongside conventional sensors (LiDAR, RGB and depth cameras, radar and IMU), both RSUs and vehicles use antenna arrays for communication. Specifically, the vehicles are modeled as users and the RSUs as BSs.

In what follows, we first give the general framework of the dataset to illustrate how we generate data. Then, we introduce the parametric details of all modalities in the dataset and how they correspond with our multimodal LLM-based beam prediction task. Notably, the following content serves as a brief introduction to the Multimodal-Wireless dataset, and readers are referred to [1] for a complete and detailed account. The dataset is publicly available in <https://le-liang.github.io/mmw/>.

A. Generation Workflow

The dataset’s generation pipeline combines CARLA [27], the autonomous driving simulator, Sionna [28], the ray-tracing engine, and Blender [29], the physical modeling software, to ensure spatial and temporal consistency across platforms. Blender acts as a bridge to replicate CARLA’s dynamic scenes in Sionna’s ray-tracing environment, ensuring all modalities share a unified world. The process, as illustrated in Fig. 5, comprises the following stages:

- **Scenario Execution and Data Capture in CARLA:** We first define and execute our scenario in CARLA. For each frame, five types of sensory data (LiDAR, RGB and depth camera, radar, and IMU) are captured. During the simulation, the dynamic state of each frame is recorded in a configuration file, consisting of the position and rotation of all vehicles in the scenario.
- **Scenario Reconstruction in Blender:** The static town map from CARLA is first established in Blender as a base environment. Then, for each frame, the pose information from its configuration file is used to place and orient all dynamic actors within this environment programmatically. Each fully constituted frame is then exported as a self-contained Sionna scene.
- **Channel Generation in Sionna:** Finally, the exported scenes are sequentially loaded into Sionna. The transmitter and receiver locations for each link are configured based on the pose data in the configuration files. Sionna’s ray-tracing engine computes the detailed channel impulse response and path parameters, which constitute the communication modality for the Multimodal-Wireless dataset.

B. Communication Modality

With the dynamic scenarios fully reconstructed in a Sionna-compatible format, Sionna serves as the ray-tracing engine to generate the multi-path channel within the scenes from Blender. This subsection provides a detailed account of the technical procedures and the channel parameters involved.

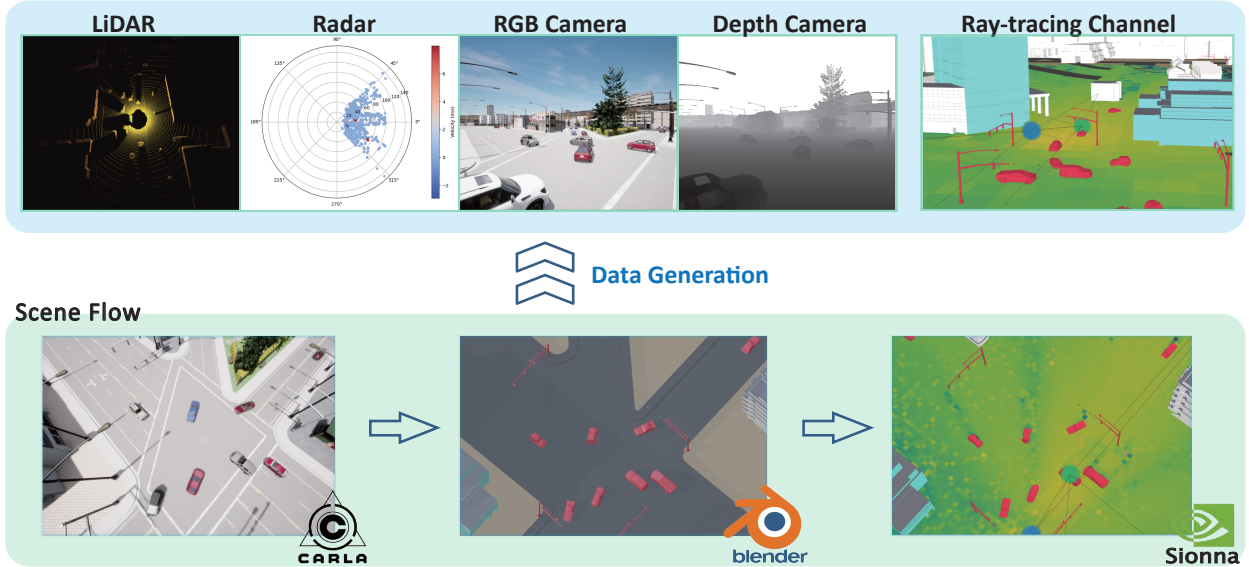


Fig. 5. Cross-platform data generation workflow for the Multimodal-Wireless dataset.

In our primary setup, we consider the communication link from the RSU to the vehicles, which serve as the mobile users. Notably, this framework is inherently extensible to vehicle-to-vehicle communications. For the channel computation, we equip the RSU with a ULA of N_t transmit antennas and each vehicle with a ULA of N_r receive antennas for 2D settings and a uniform planar array (UPA) for 3D settings. After defining the antenna patterns and polarization, Sionna's ray-tracing engine is invoked to compute the propagation paths.

To balance physical accuracy with computational feasibility, we collect the LOS path and all first-order reflection events. For each of the L resulting paths, we store its fundamental physical properties: the azimuth and zenith AoD and angles-of-arrival AoA ($\phi_l^{a/z}$, $\theta_l^{a/z}$), the propagation delay τ_l , and the complex gain matrix $\mathbf{A}_l \in \mathbb{C}^{N_r \times N_t}$, representing the complex gain of the l -th path at the carrier frequency f_c .

The fundamental multi-path parameters, especially ($\{\mathbf{A}_l\}_{l=1}^L, \{\tau_l\}_{l=1}^L$), allow us to generate custom single-carrier or multi-carrier (e.g., OFDM) frequency-domain channels by coherently summing the contributions of all paths at frequency f_k , according to the relationship:

$$\mathbf{H}(f_k) = \sum_{l=1}^L \mathbf{A}_l e^{-j2\pi f_k \tau_l}, \quad (26)$$

where $\mathbf{H}(f_k)$ is the channel frequency response at the k -th subcarrier.

All simulation parameters of Multimodal-Wireless are summarized in Table I. We categorize them into two groups: **ray-tracing parameters**, which are set during the physics-based ray-tracing process, and **communication parameters**, which can be customized by the user when synthesizing the frequency-domain channel from the raw path data ($\{\mathbf{A}_l, \tau_l\}_{l=1}^L$). This mechanism grants users maximum control over the final channel realization.

Notably, we utilize 2D data collected with 1×64 ULA in the BS and 1×16 ULA in the user for model training

TABLE I
SIONNA SIMULATION PARAMETERS IN MULTIMODAL-WIRELESS.

	Parameter	Value
Ray-tracing	Carrier Frequency	28 GHz / 4.9 GHz
	Antenna Pattern	Dipole
	Ray Samples Launched	10^6
	Maximum Reflection Order	1
	Polarization	Vertical
	Frame Duration	10 ms
Communication	Subcarrier Spacing	120 kHz
	Number of Subcarriers	1024
	Transmit Array Size	$1 \times 4/16/64/256$ (2D) / 8×8 (3D)
	Receive Array Size	$1 \times 4/16$ (2D) / 8×8 (3D)
	Number of Transmit Antennas	$4/16/64/256$ (2D) / 64 (3D)
	Number of Receive Antennas	$4/16$ (2D) / 64 (3D)

and testing. Thus, this model aligns with the multi-path channel formulation in (1), where the per-path matrix $\mathbf{A}_{n,l}$ encapsulates the path gain and spatial signatures by

$$\mathbf{A}_l = \sqrt{\frac{N_t N_r}{L}} \alpha_l \mathbf{a}_r(\theta_l^z) \mathbf{a}_t^H(\phi_l^z), \quad (27)$$

where θ_l^z and ϕ_l^z denote the dumped zenith AoA and AoD, respectively, corresponding to the 2D AoA and AoD of 2D scenarios in (1).

C. Sensor Modality

In the CARLA simulator, all sensory data are collected at a base sampling rate of 100 Hz. This high-frequency data acquisition ensures that a detailed raw data stream is available, from which users are allowed to downsample to any practical frequency that is suitable for their specific application. In this subsection, we present the configuration of the sensors and the physics-based weather impairment modeling employed to enhance data fidelity.

1) *Sensor Configuration and Specifications*: Multimodal-Wireless utilizes two distinct sensor-equipped platforms: vehicles and RSUs. Each vehicle is equipped with a sensor suite that includes four RGB cameras. These cameras are positioned to face the front, back, left, and right, thereby providing full 360-degree visual coverage around the vehicle. Beyond the cameras, each vehicle is also equipped with a LiDAR sensor and an IMU. The RSUs are outfitted with a different set of sensors, with each unit containing an RGB camera, a depth camera, a LiDAR, and a radar. In our network, we utilize the LiDAR and RGB camera modality as sensing data.

However, the perception ranges of these sensor types vary significantly, as illustrated in Fig. 6, which also shows a schematic trajectory of a vehicle moving through the environment. Typically, the effectiveness of the RSU camera and radar is constrained by a limited field of view (FOV). Consequently, these two sensors only detect the vehicle in a part of the overall scenario. In contrast, the LiDAR on the RSU can sense the vehicle across the entire area. The detailed technical specifications for all of these sensors are provided in Table II.

2) *LiDAR Weather Impairment Modeling*: While the CARLA simulator provides high-fidelity visual rendering for adverse weather, its native LiDAR sensor operates based on geometric ray-casting and does not physically interact with environmental particles. To bridge the gap between simulation and real-world sensing, we implement a physics-based post-processing pipeline to synthesize realistic weather-induced impairments on the raw LiDAR data.

Fog Simulation: Following the optical model in [30], we simulate the impact of fog through two mechanisms: *hard target attenuation* and *soft target backscattering*. Based on the Beer-Lambert law, the intensity of points reflected from solid objects is exponentially attenuated according to the distance and fog density. This attenuation process is formulated as:

$$I_{\text{fog}} = I_0 \cdot e^{-2\alpha_{\text{fog}}R}, \quad (28)$$

where I_{fog} is the received intensity from the hard target in foggy conditions, I_0 represents the intensity in clear weather, R denotes the radial distance to the target, and α_{fog} is the fog extinction coefficient. The factor 2 accounts for the round-trip path of the laser beam. Furthermore, to simulate the ‘‘screen effect’’ where fog itself reflects laser beams, we introduce phantom points (soft targets) by querying a pre-calculated backscattering intensity table. If the fog backscattering intensity I_{bck} exceeds the attenuated object return I_{fog} , the point is characterized as a fog point, introducing realistic spatial noise and occlusion.

Rain Simulation: For rainy scenarios, we adopt the parametric model from [31] to inject three distinct physical artifacts based on the rainfall rate r (mm/h): *distance perturbation*, *intensity attenuation*, and *point dropping*. To model the refraction and scattering variance, Gaussian noise is added to the radial distance of each point. The perturbed distance R' is modeled as $R' = R + \epsilon$, where $\epsilon \sim \mathcal{N}(0, \sigma_0^2)$ represents the range error, with the variance σ_0^2 scaling with r . Concurrently, signal intensity is attenuated to reflect energy loss through the rain medium. According to the empirical relationship between

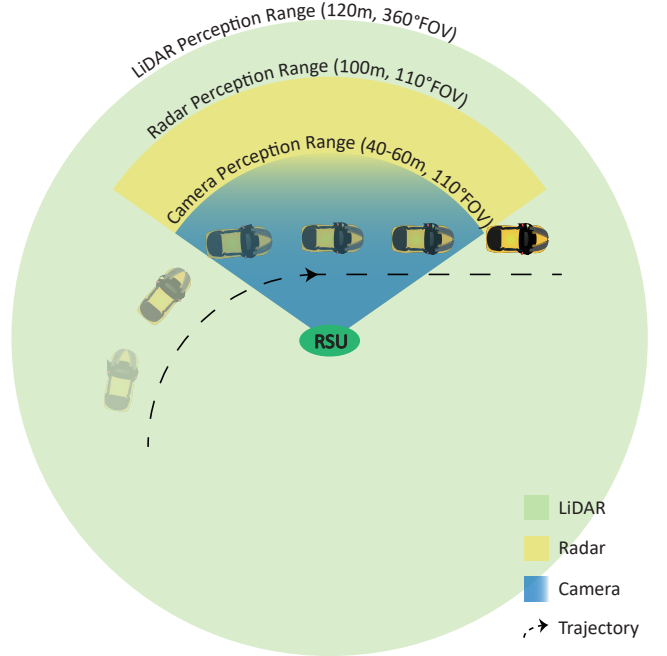


Fig. 6. Illustration of sensor perception ranges with vehicle trajectory.

the rain extinction coefficient α_{rain} and the rainfall rate r , the attenuation is formulated as:

$$\alpha_{\text{rain}} = \beta \cdot r^b, \quad I_{\text{rain}} = I_0 \cdot e^{-2\alpha_{\text{rain}}R}, \quad (29)$$

where β and b are empirical constants depending on the laser wavelength, and I_{rain} denotes the reduced intensity in rain. Finally, a sensitivity threshold I_{th} is applied to filter out points with intensity falling below the detectable limit ($I_{\text{rain}} < I_{\text{th}}$), accurately reproducing the reduced detection range and sparsity observed in real-world rainy conditions.

TABLE II
SENSOR SPECIFICATIONS.

Sensors	Attributes
RGB Camera	640 × 480 resolution, 110° FOV
Depth Camera	640 × 480 resolution, 110° FOV
LiDAR	64 channels, 30k points per sample, 120 m capturing range, −25° to 2° vertical FOV
IMU	Gyroscope noise: mean 0.001 rad/s, standard deviation (std) 0.002 rad/s, acceleration noise: std 0.1 m/s ²
Radar	2k points per sample, 100 m capturing range, 30° vertical FOV and 110° horizontal FOV

V. SIMULATION RESULTS

A. Dataset and Setup

We conduct our experiments using the Multimodal-Wireless dataset. It provides synchronized data streams from multiple sensors, including LiDAR and camera, along with communication channel information generated via precise ray-tracing. For our study, we primarily utilize the data collected under the ‘‘sunny’’ weather scenario. We utilize a total of 50 trajectories, 40 used for training (41, 800 samples), 5 for validation (6, 000

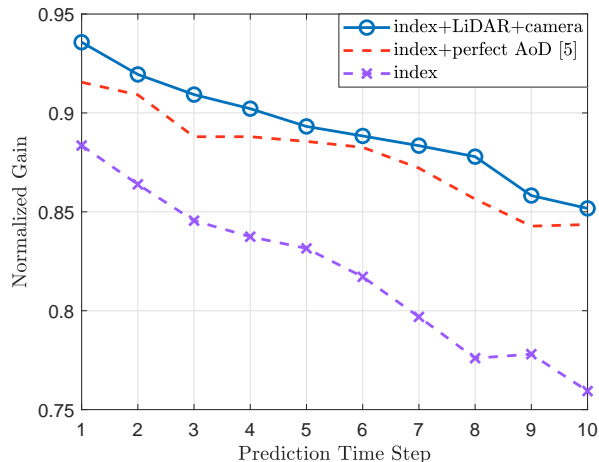


Fig. 7. Prediction performance of the proposed multimodal LLM-based method compared with the method in [5].

samples), and the remaining 5 for testing (6,000 samples). By strictly separating the trajectories across these sets, we ensure a disjoint split, meaning all reported results reflect the model’s generalization capability in out-of-distribution settings. The BSs are equipped with 1×64 ULAs, setting N_t to be 64, whereas the users are equipped with 1×16 ULAs, with $N_r = 16$. The size of the beam codebook Q for the BSs and users is set to 64. The time resolution for each prediction step is 10 ms. For user mobility, the vehicle speed is not constant but varies adaptively according to traffic conditions, ranging from static positioning in traffic jams to high-speed cruising on clear avenues. This variability helps mitigate the risk of overfitting and endows the model with inherent robustness to speed fluctuations.

The system environment of the server is Ubuntu 22.04, with Python 3.8. The graphics card utilized is the NVIDIA GeForce RTX 4090 24 GB GPU.

B. Model and Baselines

We configure our model with a look-back window of $P = 40$ time steps (i.e., 400 ms) and a prediction horizon of $W = 10$ time steps (i.e., 100 ms). For the core of our architecture, we employ a pre-trained GPT-2 model [32] as the LLM backbone. This choice strikes a balance between robust reasoning capabilities and practical inference speed. To demonstrate the practical superiority of our approach, we compare our proposed multimodal model—which relies on readily accessible, on-site LiDAR and camera data—directly against the original baseline from [5], which assumes the availability of perfect AoD knowledge.

C. Numerical Results

Fig. 7 compares the performance of the proposed multimodal LLM-based method with the LLM-based approach in [5], evaluated in terms of the normalized gain defined in (6). The baseline model is trained on the same dataset, leveraging beam indices and perfect AoD for long-term beam prediction. A practical baseline trained with only historical indices is also

included. As shown in Fig. 7, by incorporating LiDAR and camera data, our multimodal LLM-based method consistently achieves close normalized gain with the AoD-based method in [5] across all prediction time steps, effectively solving the severe performance degradation caused by the absence of practically unavailable perfect AoD. This improvement arises because historical LiDAR and camera data provide valuable environmental context, allowing the model to better capture scene dynamics such as incoming traffic jams and more accurately predict subsequent indices.

To evaluate the model performance from a classification perspective, we employ the Top- k beam accuracy, which measures the probability that the predicted beam index, \hat{q}_m , is successfully included within the set of k candidates with the highest normalized gains, denoted as $\mathcal{S}_{m,i}^{(k)}$. Mathematically, it is defined as:

$$\text{Acc}_m @ k = \frac{1}{N_{\text{test}}} \sum_{i=1}^{N_{\text{test}}} \mathbb{1}(\hat{q}_m \in \mathcal{S}_{m,i}^{(k)}), \quad (30)$$

where $\mathbb{1}(\cdot)$ is the indicator function, which equals 1 if the condition is true and 0 otherwise. As illustrated in Fig. 8, we compare the Top-1 and Top-3 accuracy of our multimodal method against the baseline with perfect historical AoD. First, the Top-3 accuracy for both methods remains consistently near 1.0 across the entire prediction horizon. This indicates that even when the model misses the exact optimal beam (causing the decay in the Top-1 curve), the true optimal beam or a highly correlated neighbor is almost always present in the Top-3 suggestions. This suggests that the uncertainty of the LLM is well-confined within a narrow angular sector. Second, our multimodal method consistently outperforms the AoD-based baseline in the Top-1 regime, particularly at later time steps (e.g., $m = 10$). This reinforces the conclusion that multimodal sensory data provides superior context for anticipating complex user mobility compared to historical channel geometry alone. In practice, this implies that by slightly increasing the overhead to sweep just 3 predicted beams, the system can eliminate the performance degradation caused by prediction errors, ensuring highly reliable connectivity.

We benchmark our approach against LSTM [33] and ResNet [34] baselines, both scaled up to match the parameter magnitude of the proposed LLM to ensure fairness. Table III reveals a compelling finding: despite our GPT2-based model incurring the highest computational complexity in terms of floating point operations (FLOPs), it demonstrates superior inference speed compared to the baselines. This efficiency stems from the highly parallel nature of the Transformer architecture, which effectively utilizes GPU resources. For real-time deployment, although the inference latency exceeds the single-step interval of 10 ms, this can be addressed via pipeline optimization or by directly leveraging the prediction horizon (e.g., applying predictions for the latter 5 steps). In terms of prediction quality, our multimodal model significantly outperforms others in Top-1 accuracy and normalized gain. This performance advantage is particularly evident in handling the dynamic vehicle speeds in our dataset, confirming the superior robustness of the LLM framework over traditional architectures.

TABLE III
MODEL COMPLEXITY ANALYSIS AND PERFORMANCE COMPARISON.
ABBREVIATIONS: **PARAM.** (PARAMETERS), **ACC.** (ACCURACY), **AVG.** (AVERAGE) AND **NORM.** (NORMALIZED).

Model	Param. (M)	FLOPs (G)	Inference Time (ms)	Avg. Top-1 Acc.	Avg. Norm. Gain	
LSTM	565.7	379.5	99.7	42.0%	51.3%	
ResNet	460.6	309.5	46.1	76.9%	85.3%	
GPT2	Index	754.1	488.1	34.2	72.8%	81.9%
	[5]	755.9	488.1	33.1	79.5%	87.8%
	Ours	777.0	518.6	43.5	80.8%	89.1%

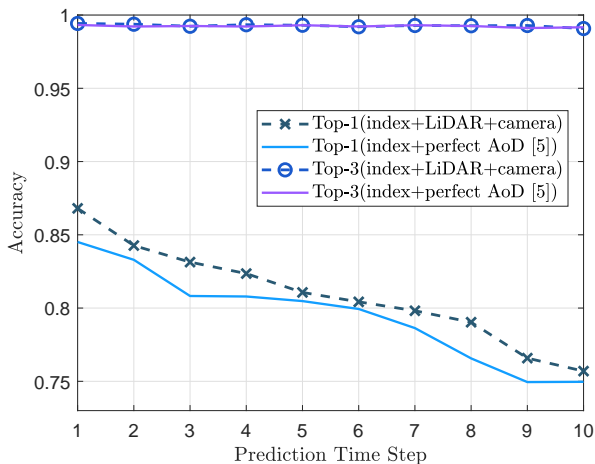


Fig. 8. Top-1 and Top-3 prediction accuracy of the proposed multimodal LLM-based method compared with the method in [5]

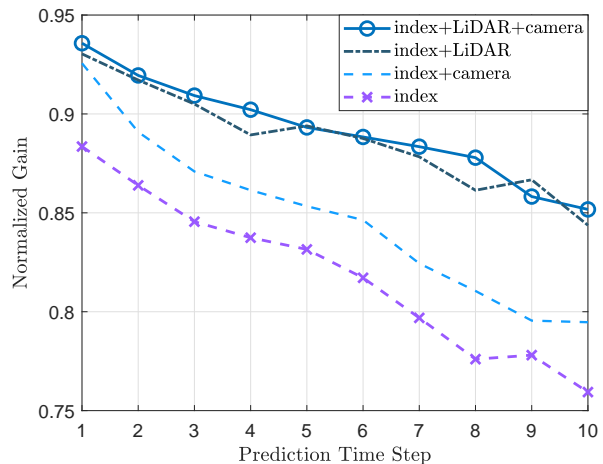


Fig. 9. Ablation study on different input modalities based on normalized gain.

For ablation study, we first investigate the contribution of different input modalities. As illustrated in Fig. 9, combining LiDAR with beam index data achieves performance close to the full-modality model, corresponding to the “index+LiDAR” curve. In contrast, removing LiDAR while retaining the camera input leads to a substantial degradation, reflected in the “index+camera” curve. This is due to the limited FOV of the RGB camera, which compromises the quality of the camera modality data. Notably, compared with the index-only baseline, the addition of the camera modality still improves performance, highlighting the effectiveness of our camera modality processing scheme.

We then perform an ablation study to investigate the effectiveness of the proposed BGAM method. Fig. 10 visualizes the impact of BGAM on the model’s spatial attention performed in (14) within the “curvyroad” scenario. As shown in Fig. 10(c), without BGAM, the attention map is highly diffuse, with the model focusing on prominent but irrelevant background structures. This lack of spatial guidance leads to a significant misalignment between the maximum attention patch and the actual location of the user, highlighting the difficulty in disambiguating the target from environmental noise. In contrast, the integration of BGAM, as illustrated in Fig. 10(d), introduces a directional prior derived from historical beam indices, effectively constraining the attention within a focused angular sector. This mechanism successfully suppresses interference from irrelevant spatial features and

accurately localizes the user, as evidenced by the alignment of the peak attention patch with the user’s position in the BEV feature map. Moreover, as shown in Fig. 11, removing BGAM leads to a substantial drop in normalized gain, yielding results comparable to the index-only model. This observation underscores the critical role of the BGAM method.

Fig. 12 shows the normalized gain evaluated on datasets with different weather scenarios, including sunny, heavy fog, and heavy rain conditions. Under sunny conditions, the camera modality provides clear visual information and leads to noticeable performance improvements. The LiDAR modality, unaffected by false echoes, delivers accurate environmental perception and significantly enhances the normalized gain. In contrast, under heavy fog, camera images become blurred and ambiguous, resulting in a small contribution. Moreover, water vapor in the air induces Mie scattering [35] and partial occlusion of laser beams, which attenuates return intensity and range while introducing short-range false echoes, thereby producing sparser and noisier LiDAR point clouds and reducing its effectiveness. However, LiDAR still provides a measurable performance gain. Under heavy rain, the images appear clearer yet darker due to the cloudiness, resulting in a further performance improvement. Meanwhile, the dense raindrops intensify false LiDAR echoes, further diminishing the performance benefit brought by LiDAR.

Finally, we evaluate the robustness of our proposed model trained with $N_t = 64$ and codebook size $Q = 64$ by testing

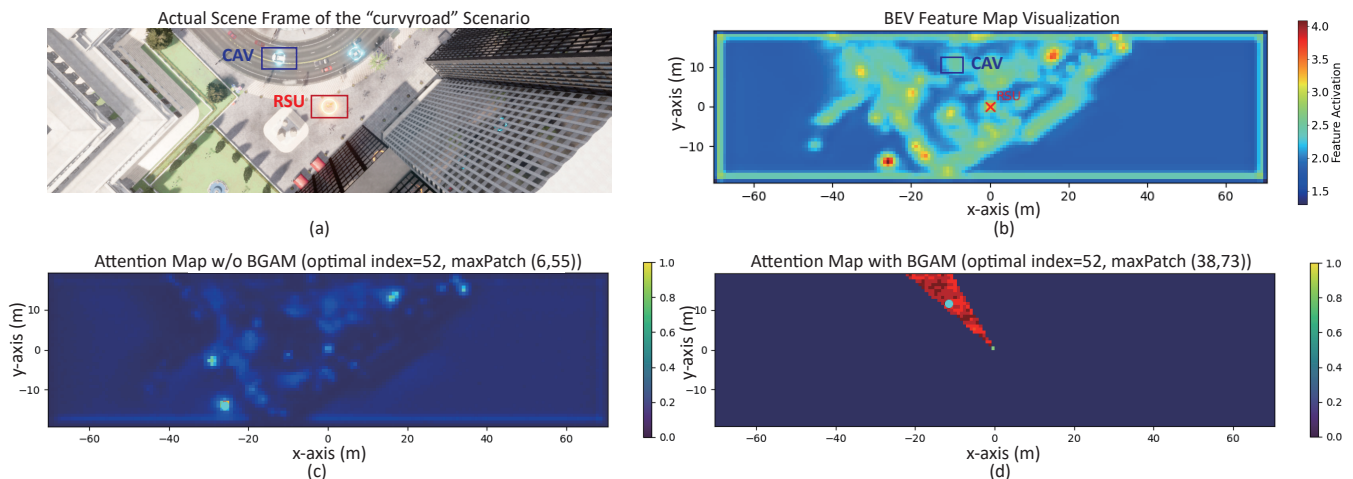


Fig. 10. Visualization of scene geometry and the effectiveness of BGAM in spatial disambiguation: (a) actual scene frame of the "curvroad" scenario with User and RSU annotations; (b) corresponding LiDAR-based BEV feature map; (c) attention map without BGAM, displaying diffuse focus and background interference; (d) attention map with BGAM, showing precise, target-specific focus guided by historical beam indices.

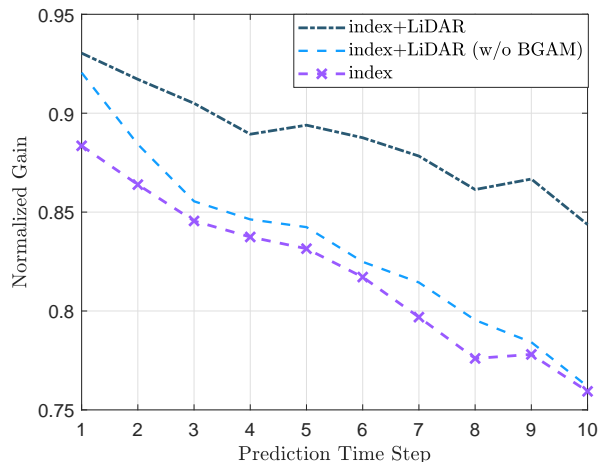


Fig. 11. Ablation study on BGAM based on normalized gain.

the model against datasets with mismatched N_t configurations, revealing the model's excellent generalization capabilities. We challenge the model with test sets generated with $N_t = 16$ and $N_t = 32$. The results, presented in Fig. 13, confirm the model's robustness to antenna configuration mismatches given that the model trained in $N_t = 64$ adapts effectively to test sets with $N_t = 16$ and 32. Moreover, the observed performance improvement with smaller N_t is expected since wider beams reduce the gain disparity between optimal and suboptimal beams.

VI. CONCLUSION

In this study, we have proposed a novel multimodal LLM-based framework for context-aware beam prediction that relies exclusively on readily available BS-side sensory data (LiDAR and RGB camera). The framework introduces two key technical innovations: (1) the BGAM mechanism, which leverages historical beam indices to dynamically guide the LiDAR encoder to focus on spatially relevant geometric features; and (2) a high-frequency temporal alignment strategy that

upsamples sensory features to preserve channel temporal resolution (100 Hz) while ensuring causality. Furthermore, we construct Multimodal-Wireless, a large-scale, high-fidelity dataset generating synchronized channel and sensing data via ray-tracing across diverse weather conditions (sunny, rainy, foggy). Simulation results demonstrate that our approach significantly outperforms state-of-the-art LLM-based baselines that assume perfect AoD knowledge, exhibiting superior robustness against adverse weather and hardware configuration mismatches.

REFERENCES

- [1] T. Mao, L. Liang, J. Yang, H. Ye, S. Jin, and G. Y. Li, "Multimodal-wireless: A large-scale dataset for sensing and communication," *arXiv preprint arXiv:2511.03220*, 2025.
- [2] F. Liu, W. Yuan, C. Masouros, J. Yuan, and T. D. Lesto, "Seventy years of radar and communications: The road from separation to integration," *IEEE Signal Process. Mag.*, vol. 40, no. 5, pp. 106–121, Jul. 2023.
- [3] G. Liang, M. Yang, D. Liu, P. Henderson, and L. Hanzo, "Environment-aware channel inference via cross-modal flow: From multimodal sensing to wireless channels," *arXiv preprint arXiv:2512.04966*, 2025.
- [4] Y. Zeng, J. Chen, J. Xu, D. Wu, X. Xu, S. Jin, X. Gao, D. Gesbert, S. Cui, and R. Zhang, "A tutorial on environment-aware communications via channel knowledge map for 6G," *IEEE Commun. Surv. Tutorials*, vol. 26, no. 3, pp. 1478–1519, Feb. 2024.
- [5] Y. Sheng, K. Huang, L. Liang, P. Liu, S. Jin, and G. Y. Li, "Beam prediction based on large language models," *IEEE Wireless Commun. Lett.*, vol. 14, no. 5, pp. 1406–1410, May 2025.
- [6] G. Charan, T. Osman, A. Hredzak, N. Thawdar, and A. Alkhateeb, "Vision-position multi-modal beam prediction using real millimeter wave datasets," in *Proc. IEEE WCNC*, 2022, pp. 2727–2731.
- [7] S. Tariq, B. E. Arfeto, U. Khalid, S. Kim, T. Q. Duong, and H. Shin, "Deep quantum-transformer networks for multi-modal beam prediction in ISAC systems," *IEEE Internet Things J.*, vol. 11, no. 18, pp. 29387–29401, Sept. 2024.
- [8] B. Shi, M. Li, M.-M. Zhao, M. Lei, and L. Li, "Multimodal deep learning empowered millimeter-wave beam prediction," in *Proc. IEEE VTC*, 2024, pp. 1–6.
- [9] Y. Cui, J. Nie, X. Cao, T. Yu, J. Zou, J. Mu, and X. Jing, "Sensing-assisted high reliable communication: A transformer-based beamforming approach," *IEEE J. Sel. Topics Signal Process.*, vol. 18, no. 5, pp. 782–795, Jul. 2024.
- [10] Z. Qin, L. Liang, Z. Wang, S. Jin, X. Tao, W. Tong, and G. Y. Li, "AI empowered wireless communications: From bits to semantics," *Proceedings of the IEEE*, vol. 112, no. 7, pp. 621–652, Aug. 2024.
- [11] K. Patel and R. W. Heath, "Harnessing multimodal sensing for multi-user beamforming in mmwave systems," *IEEE Trans. Wireless Commun.*, vol. 23, no. 12, pp. 18725–18739, Dec. 2024.

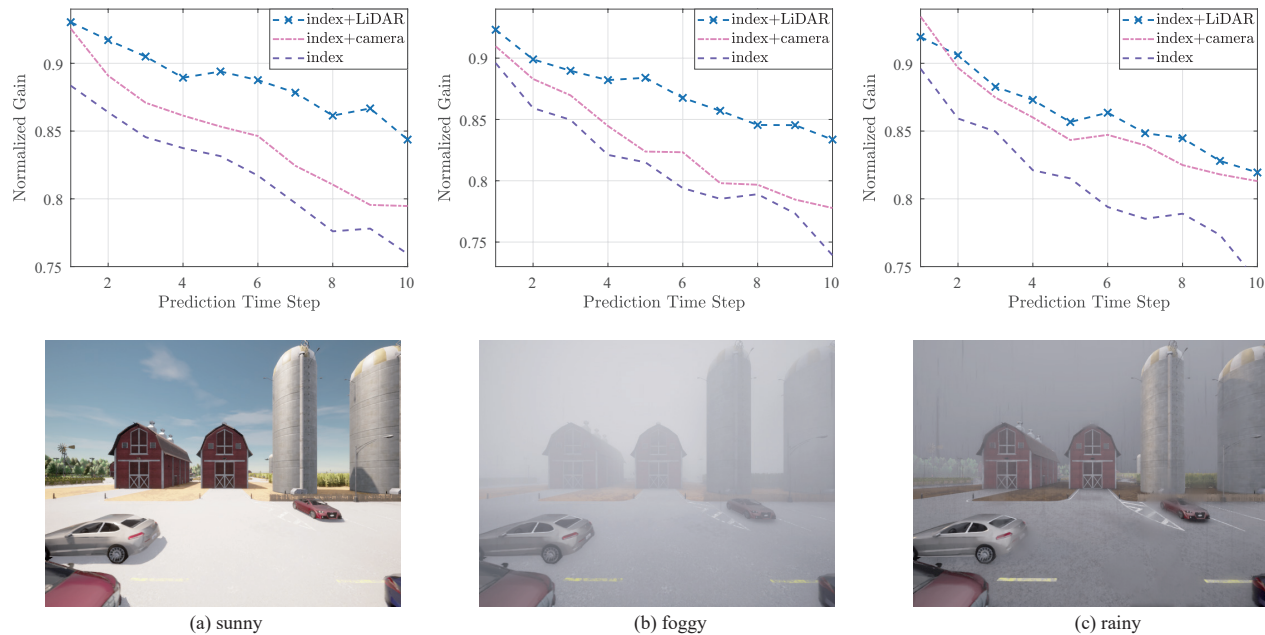


Fig. 12. Prediction performance and scene visualization under different weather conditions: (a) sunny, (b) foggy, and (c) rainy.

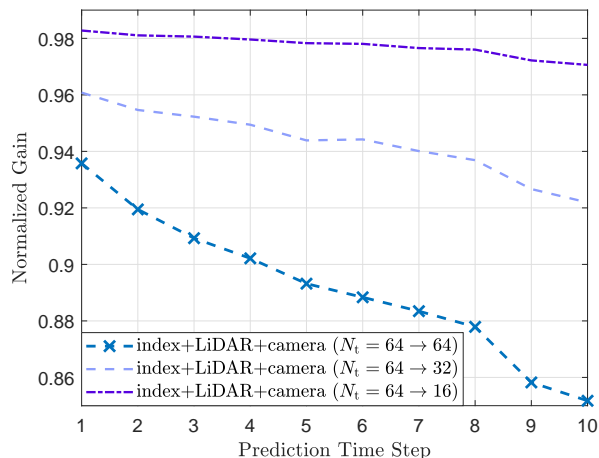


Fig. 13. Model robustness to mismatch of transmit antenna number N_t .

[12] L. Liang, H. Ye, Y. Sheng, O. Wang, J. Wang, S. Jin, and G. Y. Li, "Large language models for wireless communications: From adaptation to autonomy," *arXiv preprint arXiv:2507.21524*, 2025.

[13] A. Radford *et al.*, "Learning transferable visual models from natural language supervision," in *Proc. ICML*, 2021, pp. 8748–8763.

[14] R. Girdhar, A. El-Nouby, Z. Liu, M. Singh, K. V. Alwala, A. Joulin, and I. Misra, "Imagebind: One embedding space to bind them all," in *Proc. IEEE/CVF CVPR*, 2023, pp. 15180–15190.

[15] J. Li, D. Li, S. Savarese, and S. Hoi, "BLIP-2: bootstrapping language-image pre-training with frozen image encoders and large language models," in *Proc. ICML*, 2023.

[16] H. Jun *et al.*, "ImageBind-LLM: Multi-modality instruction tuning," *arXiv preprint arXiv:2309.03905*, 2023.

[17] R. Xu, H. Xiang, X. Xia, X. Han, J. Li, and J. Ma, "OPV2V: An open benchmark dataset and fusion pipeline for perception with vehicle-to-vehicle communication," in *Proc. IEEE ICRA*, 2022, pp. 2583–2589.

[18] H. Yu *et al.*, "DAIR-V2X: A large-scale dataset for vehicle-infrastructure cooperative 3d object detection," in *Proc. IEEE/CVF CVPR*, 2022, pp. 21361–21370.

[19] A. Alkhateeb, "DeepMIMO: A generic deep learning dataset for millimeter wave and massive MIMO applications," in *Proc. ITA*, 2019, pp.

1–8.

[20] J. Gu, B. Salehi, D. Roy, and K. R. Chowdhury, "Multimodality in mmWave MIMO beam selection using deep learning: Datasets and challenges," *IEEE Commun. Mag.*, vol. 60, no. 11, pp. 36–41, Nov. 2022.

[21] M. Alrabeiah, A. Hredzak, Z. Liu, and A. Alkhateeb, "ViWi: A deep learning dataset framework for vision-aided wireless communications," in *Proc. IEEE VTC*, Nov. 2019, pp. 1–5.

[22] A. Alkhateeb *et al.*, "DeepSense 6G: A large-scale real-world multimodal sensing and communication dataset," *IEEE Commun. Mag.*, vol. 61, no. 9, pp. 122–128, Sept. 2023.

[23] J. Yang, C. K. Wen, and S. Jin, "Hybrid active and passive sensing for SLAM in wireless communication systems," *IEEE J. Sel. Areas Commun.*, vol. 40, no. 7, pp. 2146–2163, Jul. 2022.

[24] A. H. Lang, S. Vora, H. Caesar, L. F. Zhou, J. Yang, and O. Beijbom, "PointPillars: Fast encoders for object detection from point clouds," in *Proc. IEEE/CVF CVPR*, 2019, pp. 12689–12697.

[25] C. R. Qi, H. Su, K. Mo, and L. J. Guibas, "PointNet: Deep learning on point sets for 3d classification and segmentation," in *Proc. IEEE CVPR*, 2017.

[26] A. Dosovitskiy, "An image is worth 16x16 words: Transformers for image recognition at scale," *arXiv preprint arXiv:2010.11929*, 2020.

[27] A. Dosovitskiy, G. Ros, F. Codevilla, A. M. López, and V. Koltun, "Carla: An open urban driving simulator," in *Proc. CoRL*, 2017.

[28] J. Hodyis *et al.*, "Sionna: An open-source library for next-generation physical layer research," <https://nvlabs.github.io/sionna/>, 2022, version 0.19.2.

[29] B. O. Community, *Blender a 3D modelling and rendering package*, Blender Foundation, Stichting Blender Foundation, Amsterdam, 2018. [Online]. Available: <http://www.blender.org>

[30] M. Hahner, C. Sakaridis, D. Dai, and L. Van Gool, "Fog simulation on real LiDAR point clouds for 3D object detection in adverse weather," in *Proc. IEEE/CVF ICCV*, 2021, pp. 15283–15292.

[31] C. Goodin, D. Carruth, M. Doude, and C. Hudson, "Predicting the influence of rain on LiDAR in ADAS," *Electronics*, vol. 8, no. 1, p. 89, 2019.

[32] A. Radford, J. Wu, R. Child, D. Luan, D. Amodei, and I. Sutskever, "Language models are unsupervised multitask learners," *OpenAI Blog*, vol. 1, no. 8, Feb. 2019.

[33] S. Hochreiter and J. Schmidhuber, "Long short-term memory," *Neural computation*, vol. 9, no. 8, pp. 1735–1780, 1997.

[34] K. He, X. Zhang, S. Ren, and J. Sun, "Deep residual learning for image recognition," in *Proc. IEEE/CVF CVPR*, 2016, pp. 770–778.

[35] M. Grabner and V. Kvicera, "The wavelength dependent model of extinction in fog and haze for free space optical communication," *Optics Express*, vol. 19, no. 4, pp. 3379–3389, Feb. 2011.